Utilizing diffusion kinetics of ^{3}He in quartz to constrain Holocene climate variability in Yosemite Valley

Maura Uebner
Advised by David Shuster and Marissa Tremblay

A thesis submitted in partial fulfillment of the requirements for the Degree of Bachelor of Arts with Honors in Geology

University of California, Berkeley

12 May 2017

1. Introduction

1.1 Motivation

This thesis focuses on samples from Yosemite National Park, located in the central Sierra Nevada Mountains, California. The Sierra Nevada are the primary water source for California. The state has experienced extreme drought in the past few years, and models predict that duration and severity of droughts will increase in the future, as human populations continue to grow (Mann and Glieck, 2015). An understanding of past climate fluctuations, especially on small spatial scales, provides information vital to understanding how our climate may change in the future.

The purpose of this work is to better constrain the Holocene climate of Yosemite Valley using the ^{3}He in quartz system. The samples that are the focus of this study are rockfall boulders from events that have occurred during the Holocene (Fig. 1). The diffusion kinetics of quartz from each sample location are determined below, with stepwise heating experiments. Bulk cosmogenic ^{3}He content is measured as well. With this information, we calculate the effective diffusion temperature (EDT) for several samples, and provide quantitative results regarding Holocene temperatures in Yosemite Valley.

1.2 Climate History/Existing Climate Records

Previous work has examined the Pliocene-Holocene climate of Yosemite National Park, and the Sierra Nevada in general. These include studies using pollen records, reconstruction of past lake levels, and glacial fluctuations (Mensing, 2001, Bacon et al., 2006, Blunt and Negrini, 2015, Clark and Gillespie, 1997, Phillips, 2016). Recent cosmogenic data from across the Sierra Nevada provides constraints on the Tioga glaciation, the latest stage of the LGM. The latest maximum extent is dated to 16.2 ka, and its retreat to 15.75 ka (Rood et al., 2011, Phillips, 2016). Pollen records at Owens Lake, in the Eastern Sierra Nevada, indicate a cooler and wetter climate prior to LGM retreat (Mensing, 2001). At roughly the same time as the retreat of the glaciers, and in the following few ka, a warming trend ensued, expressed in geochemical records at Moaning Cavern and Fallen Leaf Lake (Oster et

al., 2009, Noble et al., 2016). Lake levels oscillated between 15,800 and 11,400 years before present, but led to a general decline of ~38 m (Bacon et al., 2006).

A global cooling event, termed the Younger Dryas (YD) occurred between 12.9-11.6 ka (Stuiver et al., 1995). Prior work indicates that a glacial advance across North America coincided with the YD (Kennett et al., 2015). Climate records in Sierran lakes, including Swamp Lake in Yosemite NP, record a relatively cool and wet early YD, with warming and drying later in the period (MacDonald et al., 2008, Street, Anderson, and Paytan, 2012).

A brief glacial advance, locally termed the Recess Peak glaciation, was much more limited than the LGM. However, while elsewhere in North America this advance correlates with the YD, in the Sierra Nevada it appears to have occurred beforehand. ^{14}C dates indicate that the maximum extent of the Recess Peak occurred at 13.25 ka, and that retreat occurred at 12.8 ka at the latest (Phillips, 2016, Clark and Gillespie, 1997). A possible explanation for this discrepancy is the Intra-Allerød Cold Period, which took place from 13.3-13.1 ka (Stuiver et al., 1995).

Following the Recess Peak glaciation and YD, a drier climate resulted in a lowstand at Owens Lake at 11.2 ka (Bacon et al., 2006). Similarly, warming and drying are observed from 16.5-12.2 ka at Moaning Cavern (Oster et al., 2009). Within Yosemite NP, geochemical proxies point to warm summers and cool winters through 8 ka, and the fire record of the NW Great Basin supports this (Street et al., 2012, Minckley, Whitlock, and Bartlein, 2007). However, Tulare Lake, a freshwater lake at the southern end of the San Joaquin Valley, CA, shows evidence of a highstand from 10.3-7.5 ka, contrary to other evidence of a drier climate (Blunt and Negrini, 2015).

From about 7.5-3.1 ka, Swamp Lake in Yosemite NP shows general signs of warming. The period from roughly 7.5-6 ka was the driest, with decreased detrital input and organic matter recycling. After 5.5 ka, proxies show signs of increased runoff and lake levels, consistent with other work showing an increase in Sierran precipitation after 6 ka (Street et al., 2012, Minckley et al., 2007, Anderson, 1990).

Lake records from across the Sierras suggest a significant climate event prior to 3 ka. Transgressions at Owens Lake and Tulare Lake record a significant increase

in precipitation (Bacon et al., 2006, Blunt and Negrini, 2015). Similarly, both organic and inorganic proxies at Fallen Leaf Lake indicate enhanced lake mixing and cooler conditions between 4.7-3.7 ka (Noble et al., 2016). An abrupt increase in organic carbon and biomarker distributions reported by Street et al. (2012, 2013) suggest an increase in lake level and a wetter climate at Swamp Lake.

Lake records for the western and crest of the Sierra Nevada suggest that this warm, dry period ceased at about 6000 years before present, and was followed by a period of increased precipitation (Anderson, 1990). An increase in lake level at Owens Lake is seen after 4.3 ka (Bacon et al., 2006), and evidence from Swamp Lake supports regional cooling and moistening in the late Holocene (after 3.1 ka) as well (Street et al., 2012). Additionally, lichenometric ages suggest a small glacial advance at ~3 ka (Konrad and Clark, 1998), further supporting a region-wide cooling and moistening event.

A brief period of warm and dry climate between roughly 1.0-0.5 ka is recorded at Swamp Lake (Street et al., 2012). Following this, the most recent glacial advance occurred. Within the Sierra Nevada it is termed the Matthes glaciation, while it is colloquially known as the "Little Ice Age." Clark and Gillespie (1997) place its maximum extent at 700-600 years before present, and cooling at Swamp Lake is recognized around 500 years before present (Street et al., 2012). Major vegetation changes, including an increase in fires, within Yosemite Valley are observed between 750-650 years before present (Anderson and Carpenter, 1991). However, Anderson and Carpenter (1991) attribute these changes to the presence of Native American populations; they have a recorded history of burning fires and uprooting young trees to keep forests in the valley open.

Previous work utilizing a variety of proxies, including lake levels, sediment geochemistry, and ^{14}C dates provides an important background for evaluating the results of ^{3}He thermochronometry. However, these proxies are limited in providing constraints on past climate—they give a relative sense of what time periods were warmer and drier, or wetter and cooler, but provide no quantitative information. The ^{3}He in quartz system can place quantitative constraints on past temperatures, where these other systems fail. Based on the proxy record, we know that Holocene

climate has been relatively stable. However, we may expect to see small fluctuations in temperature due to the Younger Dryas, cooling at 3.5 ka, warming at 1 ka, and cooling from the Matthes glacial advance. With ^{3}He in quartz, we can obtain quantitative estimates for Holocene temperatures.

1.3 Cosmogenic Noble Gas Paleothermometry

Cosmogenic nuclides are produced in minerals in rocks at the Earth's surface, primarily from spallation reactions with secondary cosmic-ray particles, most of which are high-energy neutrons (Lal and Peters, 1967). Cosmogenic nuclides have a wide variety of applications in the Earth sciences, including determining erosion rates, exposure ages, and fault slip rates (Gosse and Phillips, 2001). ^{3}He has the highest production rate of all terrestrial cosmogenic nuclides produced *in-situ*, 116 atoms/g/yr in quartz (Vermeesch et al., 2009, rescaled using Stone, 2000). However, because it can be difficult to quantify its production rate, models, experiments, or other ^{3}He retentive phases are used to estimate it (Vermeesch et al., 2009, Masarik and Reedy, 1995, Ackert et al., 2011). Unfortunately, work utilizing this system has been limited, due to high rates of diffusion of ^{3}He in quartz at surface temperatures (Brook and Kurz, 1990). However, because its diffusion is temperature sensitive, ^{3}He can yield useful paleoclimate information if its diffusion kinetics are known.

The diffusive behavior of ^{3}He in quartz can be modeled by the Arrhenius equation

$$\frac{D(T)}{a^2} = \frac{D_0}{a^2}\, exp\left(\frac{-E_a}{RT(t)}\right) \qquad (1),$$

where $D(t)$ is the diffusivity as a function of temperature, a is the lengthscale of the diffusion domain, D_0 is the diffusivity at infinite temperature, E_a is the activation energy, R is the gas constant, and T is temperature. Unfortunately, the diffusive behavior is often complex, and Arrhenius equation parameters vary between samples, making it necessary to perform diffusion experiments (Tremblay et al., 2014b). If the distribution of ^{3}He within the grain is spatially uniform, and we assume a spherical geometry, the parameters E_a and D_0/a^2 can be determined using stepwise degassing experiments.

We can also measure bulk cosmogenic ^{3}He from aliquots of hundreds of grains of non-irradiated quartz. Assuming a production rate, we can calculate an apparent ^{3}He age, or the exposure age of a sample if all ^{3}He were retained. ^{10}Be is another cosmogenic nuclide produced in quartz, but it is not diffusively lost, so it easily can be used to determine exposure ages. Because of ^{3}He loss, the apparent age of a sample is always younger than the ^{10}Be exposure age. This difference, called retention, can be quantified:

$$\frac{apparent\ {}^{3}He\ age}{{}^{10}Be\ exposure\ age} = retention \qquad (2).$$

From the Arrhenius equation parameters, and observed retention, we can model the effective diffusion temperature (EDT) (Tremblay et al., 2014a). Because temperature at the Earth's surface oscillates on daily and yearly scales, a sample would spend a portion of its time at lower temperatures with reduced diffusivity, and a portion of its time at higher temperatures, with higher diffusivity. Diffusivity is exponentially related to temperature, so the diffusivity experienced at higher temperatures has a greater effect on the concentration of ^{3}He inside a quartz grain. Thus, the apparent diffusive temperature, or EDT, would be greater than the mean temperature for a given time period (Tremblay et al., 2014a).

1.4 Rock Avalanche Deposits in Yosemite Valley

Cosmogenic nuclides are ideal for dating rock avalanche events; samples used in this work are from rock avalanche deposits. Geologically speaking, the events are nearly instantaneous, and they expose fresh rock surfaces that were previously below the Earth's surface, and shielded from cosmogenic nuclides. Thus, accumulation of nuclides begins immediately, starting from an initial concentration of zero. Within Yosemite Valley, there are 10 large deposits that have been dated using ^{10}Be (Stock, 2013). They range in age from 13.2-1.0 ka, and happen on average every 1.2 ka (Figure 1). The longest gap between two events is just over 3 ka, but they cover the Holocene fairly well. These periodic rock avalanche events provide a useful sample set with which we can examine Holocene climate in Yosemite Valley, using ^{3}He in quartz.

2. Methods

2.1 Sample Collection and Processing

Samples were provided to us by Greg Stock, Yosemite National Park Geologist. Samples were collected from various rock avalanche deposits on the floor of Yosemite Valley that were previously dated using ^{10}Be (Stock et al., 2013). The tops of the exact same boulders were sampled for ^{3}He as were sampled for 10Be, and in most cases material collected for the ^{3}He analysis came from the exact previous sampling spot for ^{10}Be. Stock also provided shielding corrections previously measured in the field (Table 1).

After collection, samples were processed in the lab in order to separate quartz. First, rocks were mechanically broken down using a jaw crusher and disc mill. The resulting grain size from the disc mill was selected in order to try to best approximate the grain size in the original rock, while avoiding composite grains. These crushed samples were then washed to remove dust and metal fragments, then sieved to separate appropriate size fractions. The largest size fraction was then magnetically separated.

The non-magnetic separate then underwent a process called frothing, commonly used in the ceramics industry to separate quartz from feldspar (Herber, 1969). Heavy liquid separation is often inefficient at separating quartz from feldspar, due to their very similar densities. Samples were first etched in 1% HF for 30-60 minutes, then rinsed with DI water. This time period is sufficient to cause significant etching on the surface of feldspar grains, but not quartz. 15-20 drops each of eucalyptus oil and dodecylamine are added to etched samples. This coats etched feldspar in lauryl-amine, a hydrophobic substance. Carbonated water is added to this mixture, causing the hydrophobic feldspar grains to float to the top. These grains are then poured off into a separate container. Carbonated water is added repeatedly, and the float portion is poured off. Grains are recoated with eucalyptus oil and dodecylamine as needed, until nearly pure quartz is left at the bottom of the beaker. The quartz separate is then soaked and rinsed in isopropanol, and left to dry before picking.

Quartz separates are prepared for analysis using binocular optical microscopes. Grains with attached biotite and feldspar, or inclusions are removed, to ensure pure quartz for analysis. Quartz is then loaded into tantalum packets for bulk ^{3}He analysis, and crimped at both ends to prevent loss of grains.

2.2 Cosmogenic ^{3}He Observations

Cosmogenic ^{3}He concentrations are measured with a MAP 215-50 sector field mass spectrometer at the BGC Noble Gas Thermochronometry Lab. Between 90 and 130 mg of quartz are loaded into tantalum packets, and measurements are made on between 1-3 packets at a time. Samples are heated to two temperature steps, 600° and 1000° C, by laser. The ^{3}He released during each heating step is measured. Blanks and standards are also run, to calibrate and quantify uncertainties, and to determine the sensitivity of the instrument during analyses. Some samples yielded abundances of ^{3}He that were indistinguishable from the background abundance, but this still allows us to place a lower bound on EDT. It is assumed that all ^{3}He measured is cosmogenic—at surface temperatures it experiences diffusive loss, so at higher temperatures experienced during the crystallization of the batholith, no ^{3}He retention is expected. There is some ^{3}He in the atmosphere, but its abundance is so low (0.013%) that we would not expect it to make a significant difference in our measurements, and where it might, blank corrections are made.

2.3 ^{3}He Diffusion Experiments

For diffusion experiments, single quartz grains are measured and loaded into Pt-Ir packets. Quartz used in diffusion experiments was irradiated with a 220 MeV proton beam for ~5 hours at the Francis H. Burr Proton Therapy Center at the Massachusetts General Hospital (Shuster et al., 2004) in fall 2015. The irradiation was done with a total proton fluence of ~1.0*10^16 p/cm^2. This ensures uniform, high concentration of ^{3}He, and measurable results at each step of the heating process (Shuster and Farley, 2005). Each sample is heated using the same schedule, with approximately 50 steps, and two retrograde heating steps. Samples are heated to between 70° to 600° C, using a diode laser. Released gas is measured using a MAP

215-50 sector field mass spectrometer at the BGC Noble Gas Thermochronometry Lab. We continue to heat the sample until no more gas is released, ensuring that no gas remains in the quartz grain. Additionally, blanks and standards are run to calibrate and quantify uncertainties. Assuming a spherical grain geometry, equations from Fechtig and Kalbitzer (1966) are used to obtain activation energy and diffusion coefficients for each heating step.

From these parameters, an Arrhenius plot is constructed, with $1/T$ (temperature) on the x-axis and $ln(D/a^2)$, where D is diffusivity and a is the dimension of the diffusion domain, on the y-axis (Fig. 2-5). A grain showing ideal behavior would produce measurements that align along a single line, with a negative slope (Eq. 1). These plots yield several parameters of the Arrhenius equation: the slope is proportional to $-E_a$, activation energy, and the y intercept is equal to $ln(D_0/a^2)$, the pre-exponential term.

2.4 MDD Modeling and Grain Size Analysis

As mentioned above, ideal diffusive behavior produces an Arrhenius plot with points lying along a single line. However, ^{3}He in quartz often displays more complex behavior (Fig. 2-5). In these cases, the diffusive behavior can be approximated using a multiple domain diffusion (MDD) model (Tremblay et al., 2014b). The temperature and duration of each heating step from the diffusion experiment is input into the model, as well as the number of ^{3}He atoms released, and the uncertainty. The number of domains to model, a range of $ln(D_0/a^2)$ values for each domain, and a single range of E_a values are determined by the user. The MDD model then chooses the values within each range that best fit the data, assigns a fraction of gas released to each domain, and calculates the misfit. Values of E_a and $ln(D_0/a^2)$ are assigned iteratively, until misfit is minimized (Table 4).

Diffusion experiments are performed on single irradiated quartz grains, that are smaller than the quartz separate used for cosmogenic ^{3}He measurements, and grain size in the whole rock (Fig. 7). In order to quantify this difference and scale the results of the diffusion experiments, analysis was performed in order to quantify the size of grains for which bulk ^{3}He was measured, and in the whole rock. The single

grains selected for the diffusion experiments were measured individually prior to analysis. Quartz separates for each sample were sprinkled onto glass dishes, and photographed using a calibrated digital microscope (Fig. 3d). Prior to crushing, a small piece of each sample was saved in order to make a "thick section". These pieces were cut using a diamond-tipped circular saw, in order to produce a flat face. This face of the rock was then scanned, along with a ruler for scale, producing a calibrated, reflected-light image of the sawed plane (Fig. 3a).

Because the samples consist of granites and granodiorites, and quartz and feldspar appear similar in plain light, the thick section images were then taken into Adobe Photoshop, where adjustments were made to increase contrast. They were then manipulated in Adobe Illustrator, where grains that could be definitively identified as quartz were traced over and colored green (Fig 3b). This was done in order to make thresholding the image to isolate quartz grains possible—if the unedited images are used, the quartz is too similar to feldspar to isolate. However, for the sprinkle photographs, the grains present are all quartz, making this step unnecessary prior to thresholding.

The following steps apply to both the grain sprinkle photographs, and the traced thick section images. Grain photographs were imported into ImageJ, an open-source image-processing program (Rasband, 1997-2017). It allows a measurement scale to be set, which was done using the scale bar for microscope images, and ruler for scanned images. The image is subsequently thresholded, to produce a black and white image where quartz grains are black, and the background is white. The program has a "particle analysis" tool, which draws ellipses with equivalent areas, orientations, and centroids for each particle (Fig 3c). For these ellipses, it produces a table with measurements of the major and minor axes, and well as the area of each. A plugin is then used to export this table into a format readable by the next program used, CSD Corrections.

The particle analysis tool was also used to obtain an average 3D aspect ratio for grains of each sample. Twenty grains from each sample were placed on double-sided tape on a microscope slide, photographed using the calibrated digital microscope, then rotated 90° and photographed again. It was assumed that each

rotation was done about the major axis. The above process of thresholding and measurement was done for photographs of rotated grains for each sample. From these measurements, an average aspect ratio for each sample, along with its standard deviation, was calculated.

For the next program, CSD Corrections (Higgins, 2002), inputs include the table of areas, and major and minor axes for each grain from ImageJ, and a 3D aspect ratio for the sample. For each two-dimensional grain slice, stereology is used to model the major, intermediate, and minor axes of a three-dimensional grain in the whole rock. Surface areas *(SA)* and volumes *(V)* for these ellipses are calculated using the following equations:

$$SA \approx 4\pi\left[\frac{ab^{1.6}+bc^{1.6}+ca^{1.6}}{3}\right]^{\frac{1}{1.6}} \qquad (3)$$

$$V = \frac{4}{3}\pi abc \qquad (4)$$

where a, b, and c are the major, intermediate, and minor axes of each ellipse. Next, a spherically equivalent radius (r), or the radius of a sphere with the same surface area and volume, is determined from equation 4.

$$r = \frac{3}{\frac{SA}{V}} \qquad (5)$$

Finally, a mean radius for each sample is calculated from the distribution of spherically equivalent radii (a_{sample}) (Table 5).

Spherically equivalent radii are also calculated for grains used in diffusion experiments (a_{exp}). For each sample, a relationship between the two radii is developed, and used to scale the pre-exponential term, D_0/a^2, determined from the multiple domain diffusion model.

$$\frac{D_0}{{a_{exp}}^2} * \frac{{a_{exp}}^2}{{a_{sample}}^2} = \frac{D_0}{{a_{sample}}^2} \qquad (6)$$

2.5 Time-Temperature Scenario Testing

Historical temperature records were obtained for Yosemite Valley at National Weather Service station ID YPQC1, in Mariposa County (Fig. 1). Modern temperature records can be used to find the modern mean temperature and EDT,

and provide a source of comparison for experimental findings. Records begin in 1905, but are incomplete until 1907; the record described here contains average monthly temperature data for 1907-2016. For ~30 data points that contained no record, an average was taken of the same month for the two previous and two following years. For consecutive or alternating years with no data, an average was taken for the three surrounding years, disregarding the other point with no data.

Average monthly temperature from 1907 to present is plotted in Figure 2. I wrote a Matlab script to calculate diffusivities for each temperature point given D_0, E_a, and R. Experimentally determined values for D_0 and E_a for each sample are input, and diffusivities returned. An average diffusivity for the time period is calculated. This is plugged into Equation 1 as D, and other parameters remain the same. Assuming a spherical geometry, the a^2 on each side cancels out. Solving for temperature yields the EDT.

$$EDT = \frac{-E_a}{R}\left(ln\left[\frac{1}{t}\int_0^t exp\left(\frac{-E_a}{RT(t')}\right)dt'\right]\right)^{-1} \qquad (7)$$

Using an activation energy of 100 *kj/mol* and the modern temperature record, we obtain a mean EDT of 15.1°C. If climate has not varied significantly over the timescale of exposure, we would expect this EDT value from bulk ^{3}He content. Comparing this to the mean temperature for the time period, 11.8° C, yields a difference between the two (ΔT) of 3.3° C. If the amplitude of temperature fluctuations has remained constant over the timescale of exposure, subtracting this ΔT from a calculated EDT would yield mean temperature experienced by the rock.

A forward model is used to test time-temperature scenarios. Inputs include diffusion parameters, the grain size used in the diffusion experiment, data from Tables 1 and 2, and the observed retention and uncertainty. Models are run using 101 temperature steps per sample. The model calculates what retention this temperature history produces. Modeled retention is compared to the observed retention, and misfit is minimized to find the EDT.

3. Results

3.1 Cosmogenic ^{3}He apparent exposure ages and retention

Cosmogenic ^{3}He measurements were made for all five sample locations shown in Figure 1. Of these five, two samples had ^{3}He concentrations below detection limits. Measureable concentrations varied between 3.8×10^{5} to 4.3×10^{5} atoms/g, corresponding to apparent ^{3}He ages of 1542 to 1750 years (Table 2, 3). For the two samples with concentrations below detection limits, these correspond to apparent ^{3}He ages of less than 125 years. Retentions vary greatly between samples, from less than 0.02 to 0.42 (Table 3).

3.2 Diffusion Experiment results

Four different diffusion experiments were conducted, and the Arrhenius equation parameters calculated from these are within the range of previously published values (Table 4, Shuster and Farley, 2005, Tremblay et al., 2014b). However, we observe complex behavior, best explained by a three domain diffusion model (Fig. 2-5). Activation energies for these models range from 83.6 to 115.1 *kj/mol*, and the pre-exponential term, $ln(D_o/a^2)$, ranges from 5.7 to 21.9.

3.3 Scaling of Diffusion Experiment Data

In order to scale the results of the diffusion experiments, analysis of grain size in the whole rock and quartz separate used to measure cosmogenic ^{3}He was performed, discussed above in section 2.4 (Table 5). A comparison of these distributions for three samples is shown in Figure 7. The mean grain size of the quartz separate was used to scale the results of the diffusion experiment (see Eq. 6). Because this is the grain size used in cosmogenic ^{3}He measurements, it best represents the diffusion lengthscale of grains retention is calculated from.

3.4 Time-Temperature scenario testing and misfits

Forward time-temperature modeling was only performed for the two samples with complete datasets, UPC-1 and SPBRA-4. Other samples lacked diffusion experiment data, or had cosmogenic ^{3}He measurements below detection limits. With scaling, for constant-temperature scenarios, these samples yielded EDT's of 37.7° C and 35.4° C, respectively, corresponding to mean temperatures of

34.4° C and 32.1° C, given the ΔT of 3.3° C discussed above in section 2.5 (Table 6). For unscaled constant-temperature scenarios, these samples yielded EDT's of 15.0° C and 20.9° C respectively, corresponding to mean temperatures of 11.7° C and 17.6° C (Table 6, Fig. 8).

Based on the proxy record, one can also construct a temperature history to be modeled with temperature fluctuations. The Younger Dryas, a significant global cool period, began at about 12.9 ka, and ended by 11.6 ka (Stuiver et al., 1995). Although the advance of the Recess Peak glaciation does not coincide with this temporally (Phillips, 2016), there is evidence for YD cooling in Yosemite National Park, meaning this is appropriate to include in a variable temperature scenario (Street et al., 2012). Several proxies, including lake levels at Owens Lake, and the Swamp and Fallen Leaf Lake geochemical record, suggest a decrease in temperature and increase in precipitation at around 3.5 ka (Bacon et al., 2006, Street et al., 2012, 2013, Noble et al., 2016). The Swamp Lake record indicate a relatively warm and dry climate within Yosemite National Park beginning at about 1 ka (Street et al., 2012), while the Matthes glaciation maximum extent, and thus cooling, occurred between approximately 700 and 500 years before present (Clark and Gillespie, 1997).

Thus, I elected to use a temperature scenario with major shifts at 12.9, 11.6, 0.7, and 0.5 ka, and with minor shifts at 3.5 and 1.0 ka. I tested scenarios with the same average EDT as the constant-temperature scenario, and compared observed retentions with those modeled by these scenarios. The retentions produced from these models are shown in Table 7 and discussed in section 4.1. Retentions for UPC-1 are best matched with fluctuations of 4-5° C, while those for SPBRA-4 are best matched for fluctuations of 1-4° C, if average EDT is matched to that determined from a constant-temperature model.

4. Discussion

4.1 Plausible EDT scenarios

Scaled EDT calculations yield results that are unreasonable for this time period, 37.7° C and 35.4° C. Instead, unscaled results are considered below as the

most plausible. The best-fit constant EDT for sample UPC-1 (15.0° C) is in good agreement with that calculated for the modern temperature record (15.1° C), in support of a stable Holocene climate (Fig. 8). The uncertainty for the constant EDT for SPBRA-4 is outside the range of the modern value, discussed more below in section 4.2. Observed retentions are reproducible for SPBRA-4 with temperature scenarios with fluctuations of up to 5° C, if mean EDT is held constant. However, when mean EDT is held constant for UPC-1, temperature fluctuations of at least 4° C are required to produce the observed retention. There is more temperature fluctuation in the late Holocene, and so complexities of its effect on retention are likely what cause this unexpected result.

The ^{3}He in quartz system has difficulty resolving smaller fluctuations, because it only provides a mean retention for duration of exposure. Although retention is affected more by higher temperatures, small fluctuations in temperature have a minimal effect on modeled retention, and are feasible for this time period, in support of a stable Holocene climate.

4.2 Limitations and uncertainties

Although the uncertainty for the constant-temperature EDT for sample SPBRA-4 is outside the modern value, this doesn't necessarily mean the result is unreasonable or incorrect. The forward time-temperature model used above doesn't take into account differential heating between the air and the rock itself. Often, rock surfaces can get significantly warmer than the surrounding air, and experience higher amplitude temperature fluctuations.

Within Yosemite Valley, rock surfaces have been documented to reach temperatures of over 40° C (Collins and Stock, 2016). Both the higher temperatures and higher amplitude would increase the apparent EDT experienced by the rocks. Additionally, there is evidence in the proxy record for higher amplitude seasonal temperature fluctuation, such as between 10.5-8 ka (Street et al., 2012), which could also increase the apparent EDT. Of these options, differential rock heating seems most likely, as only one of the two samples is affected. Thus, SPBRA-4 may experience more solar heating than UPC-1, resulting in a higher observed EDT.

The size of grains used for diffusion experiments is smaller than the mean size of those used in determining cosmogenic ^{3}He ages, and the mean whole-rock grain size (Fig. 7). Thus, the diffusion lengthscale (a^2) for the diffusion experiments is smaller than that of the majority of the grains that sat at the Earth's surface, accumulating cosmogenic ^{3}He, and those we measured ^{3}He in. Initially, we thought it would be most appropriate to scale the results of the diffusion experiment to either the mean size of grains used in cosmogenic ^{3}He measurements, or the mean grain size in the whole rock (Eq. 6). In doing this scaling, grains were modeled as ellipses, and a sphere with the same surface area:volume ratio was found (see section 2.4).

However, when this scaling was used in the forward time-temperature model discussed above, it yielded unreasonable high EDT's for the Holocene, near 40° C (Table 6). Although an EDT slightly higher than the modern value could be explained by differential heating of rocks, a discrepancy this large seems unlikely. Furthermore, when the results of the MDD model were not scaled, they yielded EDT's much more similar to the modern value, and one sample (UPC-1) had a value practically the same value (Table 6).

Modeling quartz separate and whole-rock grains as ellipses did not provide satisfactory results for these samples. Often, the spherically equivalent radius was longer than the minor axis of the corresponding ellipse, meaning the diffusion lengthscale for the sphere is longer than the minimum of the ellipse. It appears that modeling grains as prisms may provide more reasonable results. Due to time constraints I was unable to attempt this scaling, but this should be investigated for future work.

Additionally, uncertainties in the production rate of ^{3}He (116 ± 12 atoms/g/yr) were taken into account while calculating uncertainties in exposure ages, but not for the EDT. This adds another source of ambiguity not accounted for. Although grain size distributions used in determining the EDT for this time period provided unreasonable results that were disregarded, whole-rock grain size distributions are likely skewed to be larger than they truly are. In thick section, it can be difficult to distinguish whether large patches of quartz are a single grain or composed of multiple grains. Furthermore, the resolution of the scanner limits the

minimum grain size than can be identified.

4.3 Future work

Where other proxies cannot provide quantitative information on past temperatures, the ^{3}He in quartz system succeeds. However, the use of cosmogenic noble gas paleothermometry is better suited to questions about general climate trends than small-scale fluctuations. It has proved useful in quantifying general Holocene trends within Yosemite Valley, but in future work, the complexity of past climate should be considered.

Within the Sierra Nevada, if workers hope to quantify later Holocene temperatures, they should seek higher-altitude samples that have experienced lower temperatures. Our younger samples had ^{3}He concentrations below detection limits, but samples of the same age at higher elevations may yield measurable amounts. Comparing EDT's of samples with a variety of exposure ages, or samples with similar exposure histories at a variety of elevations, could reveal more information.

In considering future sampling locations, one might also consider adding instrumentation to measure rock temperatures at a sample site near a weather station. Quantifying rock surface temperatures, and their relationship with ambient air temperature, would improve confidence in the ΔT used to scale EDT to past mean temperature.

5. Conclusions

The two samples with complete datasets yield a mean EDT of 18.0° C, corresponding to a mean Holocene temperature of 14.7° C, if diffusion experiments are not scaled by grain size. However, sample UPC-1 is within uncertainty of the modern EDT, with a suggested average temperature of 11.7° C, and likely provides a more accurate record of Holocene climate. Small fluctuations in temperature are also allowable over the duration of exposure. This work could be improved with a better understanding of how best to scale the results of diffusion experiments, and site-specific information on how rock temperature relates to air temperature.

Although the ^{3}He in quartz system shows complex behavior that varies between samples, these complexities can be resolved experimentally, and ultimately provide quantitative information on past surface temperatures.

References

Ackert, R. P., Mukhopadhyay, S., Pollard, D., DeConto, R. M., Putnam, A. E., & Borns, H. W. (2011). West Antarctic Ice Sheet elevations in the Ohio Range: Geologic constraints and ice sheet modeling prior to the last highstand. *Earth and Planetary Science Letters*, *307*(1), 83-93.

Anderson, R. S. (1990). Holocene forest development and paleoclimates within the central Sierra Nevada, California. *The Journal of Ecology*, 470-489.

Anderson, R. S., & Carpenter, S. L. (1991). Vegetation change in Yosemite Valley, Yosemite National Park, California, during the protohistoric period. *Madrono*, 1-13.

Bacon, S. N., Burke, R. M., Pezzopane, S. K., & Jayko, A. S. (2006). Last glacial maximum and Holocene lake levels of Owens Lake, eastern California, USA. *Quaternary Science Reviews*, *25*(11), 1264-1282.

Balco, G., Stone, J. O., Lifton, N. A., & Dunai, T. J. (2008). A complete and easily accessible means of calculating surface exposure ages or erosion rates from 10 Be and 26 Al measurements. *Quaternary geochronology*, *3*(3), 174-195.

Blunt, A. B., & Negrini, R. M. (2015). Lake levels for the past 19,000 years from the TL05-4 cores, Tulare Lake, California, USA: Geophysical and geochemical proxies. *Quaternary International*, *387*, 122-130.

Brook, E. J., & Kurz, M. D. (1993). Surface-exposure chronology using in situ cosmogenic 3He in Antarctic quartz sandstone boulders. *Quaternary Research*, *39*(1), 1-10.

Clark, D. H., & Gillespie, A. R. (1997). Timing and significance of late-glacial and Holocene cirque glaciation in the Sierra Nevada, California. *Quaternary International*, *38*, 21-38.

Collins, B. D., & Stock, G. M. (2016). Rockfall triggering by cyclic thermal stressing of exfoliation fractures. *Nature Geoscience*.

Fechtig, H., & Kalbitzer, S. (1966). The diffusion of argon in potassium-bearing solids. In *Potassium argon dating* (pp. 68-107). Springer Berlin Heidelberg.

Gosse, J. C., & Phillips, F. M. (2001). Terrestrial in situ cosmogenic nuclides: theory and application. *Quaternary Science Reviews*, *20*(14), 1475-1560.

Herber, L. J. (1969). Separation of feldspar from quartz by flotation. *AMERICAN MINERALOGIST*, *54*(7-8), 1212.

Higgins, M. D. (2002). Closure in crystal size distributions (CSD), verification of CSD calculations, and the significance of CSD fans. *American Mineralogist*, *87*(1), 171-175.

Kennett, J. P., Kennett, D. J., Culleton, B. J., Tortosa, J. E. A., Bischoff, J. L., Bunch, T. E., ... & Goodyear, A. C. (2015). Bayesian chronological analyses consistent with synchronous age of 12,835–12,735 Cal BP for Younger Dryas boundary on four continents. *Proceedings of the National Academy of Sciences*, *112*(32), E4344-E4353.

Konrad, S. K., & Clark, D. H. (1998). Evidence for an early Neoglacial glacier advance from rock glaciers and lake sediments in the Sierra Nevada, California, USA. *Arctic and Alpine Research*, 272-284.

Lal, D., & Peters, B. (1967). Cosmic ray produced radioactivity on the earth. In *Kosmische Strahlung II/Cosmic Rays II* (pp. 551-612). Springer Berlin Heidelberg.

MacDonald, G. M., Moser, K. A., Bloom, A. M., Porinchu, D. F., Potito, A. P., Wolfe, B. B., ... & Orme, A. J. (2008). Evidence of temperature depression and hydrological variations in the eastern Sierra Nevada during the Younger Dryas stade. *Quaternary Research*, *70*(2), 131-140.

Mann, Michael E., and Peter H. Gleick. "Climate change and California drought in the 21st century." *Proceedings of the National Academy of Sciences* 112.13 (2015): 3858-3859.

Masarik, J., & Reedy, R. C. (1995). Terrestrial cosmogenic-nuclide production systematics calculated from numerical simulations. *Earth and Planetary Science Letters*, *136*(3-4), 381-395.

Mensing, S. A. (2001). Late-glacial and early Holocene vegetation and climate change near Owens Lake, eastern California. *Quaternary Research*, *55*(1), 57-65.

Minckley, T. A., Whitlock, C., & Bartlein, P. J. (2007). Vegetation, fire, and climate history of the northwestern Great Basin during the last 14,000 years. *Quaternary Science Reviews*, *26*(17), 2167-2184.

Noble, P. J., Ball, G. I., Zimmerman, S. H., Maloney, J., Smith, S. B., Kent, G., ... & Driscoll, N. (2016). Holocene paleoclimate history of Fallen Leaf Lake, CA., from geochemistry and sedimentology of well-dated sediment cores. *Quaternary Science Reviews*, *131*, 193-210.

Oster, J. L., Montañez, I. P., Sharp, W. D., & Cooper, K. M. (2009). Late Pleistocene California droughts during deglaciation and Arctic warming. *Earth and Planetary Science*

Letters, *288*(3), 434-443.

Phillips, F. M. (2016). Cosmogenic nuclide data sets from the Sierra Nevada, California, for assessment of nuclide production models: I. Late Pleistocene glacial chronology. *Quaternary Geochronology*, *35*, 119-129.

Rasband, W.S., ImageJ, U. S. National Institutes of Health, Bethesda, Maryland, USA, https://imagej.nih.gov/ij/, 1997-2017.

Rood, D. H., Burbank, D. W., & Finkel, R. C. (2011). Chronology of glaciations in the Sierra Nevada, California, from 10 Be surface exposure dating. *Quaternary Science Reviews*, *30*(5), 646-661.

Shuster, D. L., Farley, K. A., Sisterson, J. M., & Burnett, D. S. (2004). Quantifying the diffusion kinetics and spatial distributions of radiogenic 4 He in minerals containing proton-induced 3 He. *Earth and Planetary Science Letters*, *217*(1), 19-32.

Shuster, D. L., & Farley, K. A. (2005). Diffusion kinetics of proton-induced 21 Ne, 3 He, and 4 He in quartz. *Geochimica et Cosmochimica Acta*, *69*(9), 2349-2359.

Stock, G. M. (2013, October). Cosmogenic Beryllium-10 exposure dating of probable coseismic rock avalanches in Yosemite Valley, California. In *2013 GSA Annual Meeting in Denver*.

Stone, J. O. (2000). Air pressure and cosmogenic isotope production. *Journal of Geophysical Research: Solid Earth*, *105*(B10), 23753-23759.

Street, J. H., Anderson, R. S., & Paytan, A. (2012). An organic geochemical record of Sierra Nevada climate since the LGM from Swamp Lake, Yosemite. *Quaternary Science Reviews*, *40*, 89-106.

Street, J. H., Anderson, R. S., Rosenbauer, R. J., & Paytan, A. (2013). n-Alkane evidence for the onset of wetter conditions in the Sierra Nevada, California (USA) at the mid-late Holocene transition,~ 3.0 ka. *Quaternary Research*, *79*(1), 14-23.

Stuiver, M., Grootes, P. M., & Braziunas, T. F. (1995). The GISP2 δ18O climate record of the past 16,500 years and the role of the sun, ocean, and volcanoes. *Quaternary Research*, *44*(3), 341-354.

Tremblay, M. M., Shuster, D. L., & Balco, G. (2014a). Cosmogenic noble gas paleothermometry. *Earth and Planetary Science Letters*, *400*, 195-205.

Tremblay, M. M., Shuster, D. L., & Balco, G. (2014b). Diffusion kinetics of 3 He and 21 Ne in quartz and implications for cosmogenic noble gas paleothermometry. *Geochimica et Cosmochimica Acta*, *142*, 186-204.

Vermeesch, P., Baur, H., Heber, V. S., Kober, F., Oberholzer, P., Schaefer, J. M., ... & Wieler, R. (2009). Cosmogenic 3 He and 21 Ne measured in quartz targets after one year of exposure in the Swiss Alps. *Earth and Planetary Science Letters*, *284*(3), 417-425.

Tables

Sample	*Latitude*	*Longitude*	*Elevation (masl)*	*Thickness (cm)*	*Density (g/cc)*	*Shielding correction*	*Erosion rate (cm/yr)*
UPC-1	37.73265545	-119.5608106	1226	4	2.65	0.918023538	0.000653
SPBRA-4	37.74430124	-119.5680774	1214	3.5	2.65	0.916487582	0.000653
TBRA-5	37.74169900	-119.5586351	1220	4	2.65	0.928297321	0.000653
MLRA-5	37.7454779	-119.5562709	1287	1.8	2.65	0.897788963	0.000653
MLRA-6	37.7458568	-119.5529363	1260	4	2.65	0.891191151	0.000653

Table 1. Sample location information used in determining ^{10}Be and ^{3}He exposure ages. Samples were collected in 2013.

Sample	*Nuclide*	*Mineral*	*Concentration (atoms/g)*	*Conc. Unc. (atoms/g)*	*Standardization*
UPC-1	He-3	quartz	404444.29	86104.38	NONE
SPBRA-4	He-3	quartz	376127.64	50145.45	NONE
TBRA-5	He-3	quartz	431785.98	84435.68	NONE
MLRA-5	He-4	quartz	30785.72787	17973.84667	NONE
MLRA-6	He-5	quartz	30785.72787	17973.84667	NONE
UPC-1	Be-10	quartz	102270.56	2256.94	07KNSTD
SPBRA-4	Be-10	quartz	106801.9	2290.92	07KNSTD
TBRA-5	Be-10	quartz	35906.25	967.3	07KNSTD
MLRA-5	Be-11	quartz	66013.18838	1631.608074	07KNSTD
MLRA-6	Be-12	quartz	9900.68601	586.2601628	07KNSTD

Table 2. ^{10}Be and ^{3}He concentrations and uncertainties measured, ^{10}Be measurements provided by Greg Stock. Concentrations are in *atoms/g* of quartz.

Sample	*3-He age (yr)*	*Uncertainty*	*10-Be age (yr)*	*Uncertainty*	*Retention*	*Uncertainty*
UPC-1	1649	382	12371	1089	0.133	0.033
SPBRA-4	1542	247	13048	1151	0.118	0.022
TBRA-5	1750	378	4122	352	0.425	0.099

MLRA-5	119	71	7461	644	0.016	0.010
MLRA-6	125	74	1130	112	0.111	0.066

Table 3. Compilation of ^{10}Be exposure ages, apparent ^{3}He exposure ages, and retentions for each sample. Ages calculated using the Lal/Stone scaling method on version 3 of the online exposure age calculator CRONUS (Balco et al., 2008). Uncertainties reported for exposure ages are from external error.

Sample	***Domain***	***E_a (kj/mol)***	***ln (D_0/a^2)***	***Gas fraction***	***Misfit***
MLRA-2	1	109.3	15.8	0.57	0.253
	2		20.0	0.26	
	3		11.5	0.17	
MLRA-5	1	90.5	10.0	0.60	0.295
	2		13.5	0.20	
	3		7.0	0.20	
SPBRA-4	1	115.1	21.9	0.57	0.22
	2		20.1	0.33	
	3		15.7	0.10	
UPC-1	1	83.6	8.3	0.61	0.29
	2		10.9	0.20	
	3		5.7	0.19	

Table 4. Results of best fit multiple domain diffusion models, for 3 domains. E_a represents the slope of the Arrhenius plot, and $ln(D_0/a_2)$ represents the y-intercepts of the line for each domain. Misfit is determined from a Monte Carlo simulation, using methods described in Tremblay et al. (2014b).

Sample	***Whole rock (mm)***	***Standard deviation (mm)***	***Quartz separate (mm)***	***Standard deviation (mm)***	***Diffusion experiment (mm)***
MLRA-2			1.1779	0.2100	0.380
MLRA-5	1.3937	0.7947	1.1516	0.2081	0.407
SPBRA-4	1.9510	1.1095	1.1793	0.2824	0.392
TBRA-5	1.3900	0.8332	0.9920	0.1770	
UPC-1	1.3514	0.7815	1.0660	0.2141	0.318

Table 5. Spherically equivalent radii and standard deviations for whole-rock, quartz

separate, and diffusion experiment grains. Diffusion experiment measurements have no standard deviation, because the measurements are from a single grain per sample.

Sample	*EDT, mean retention, unscaled (°C)*	*EDT, retention high/exposure low, unscaled (°C)*	*EDT, retention low/exposure high, unscaled (°C)*	*EDT, mean retention, scaled to qtz separate grain size (°C)*
UPC-1	15.0	12.5	18.2	37.7
SPBRA-4	20.9	19.0	23.8	35.4

Table 6. Results of constant time-temperature scenarios tested. Lower uncertainties were calculated by adding retention uncertainty and subtracting exposure age uncertainty, and upper uncertainties were calculated by subtracting retention uncertainty and adding exposure age uncertainty and misfits to observed ^{3}He retention.

UPC-1, mean EDT constant

Ending temperature *(°C)*	**7.5 ka**	**3.5 ka**	**1 ka**	**0.7 ka**	**0.5 ka**	**Retention**
15.4	+1	-0.5	+0.5	-1	+1	0.14
16.0	+2	-1.5	+1.5	-2	+2	0.14
16.5	+3	-2.5	+2.5	-3	+3	0.14
17.0	+4	-3.5	+3.5	-4	+4	0.13
17.4	+5	-4.5	+4.5	-5	+5	0.13

SPBRA-4, mean EDT constant

Ending temperature *(°C)*	**11.6 ka**	**7.5 ka**	**3.5 ka**	**1 ka**	**0.7 ka**	**0.5 ka**	**Retention**
21.3	-1	+1	-0.5	+0.5	-1	+1	0.12
21.8	-2	+2	-1.5	+1.5	-2	+2	0.12
22.3	-3	+3	-2.5	+2.5	-3	+3	0.12
22.7	-4	+4	-3.5	+3.5	-4	+4	0.12
23.1	-5	+5	-4.5	+4.5	-5	+5	0.11

Table 7. Temperature steps used in variable-temperature scenarios, along with ending (modern) temperature, and modeled retentions. Ending temperatures were determined by finding the temperature for which the mean EDT is equal to the

calculated constant EDT. Observed retention for UPC-1 is 0.13, and SPBRA-4 is 0.12.

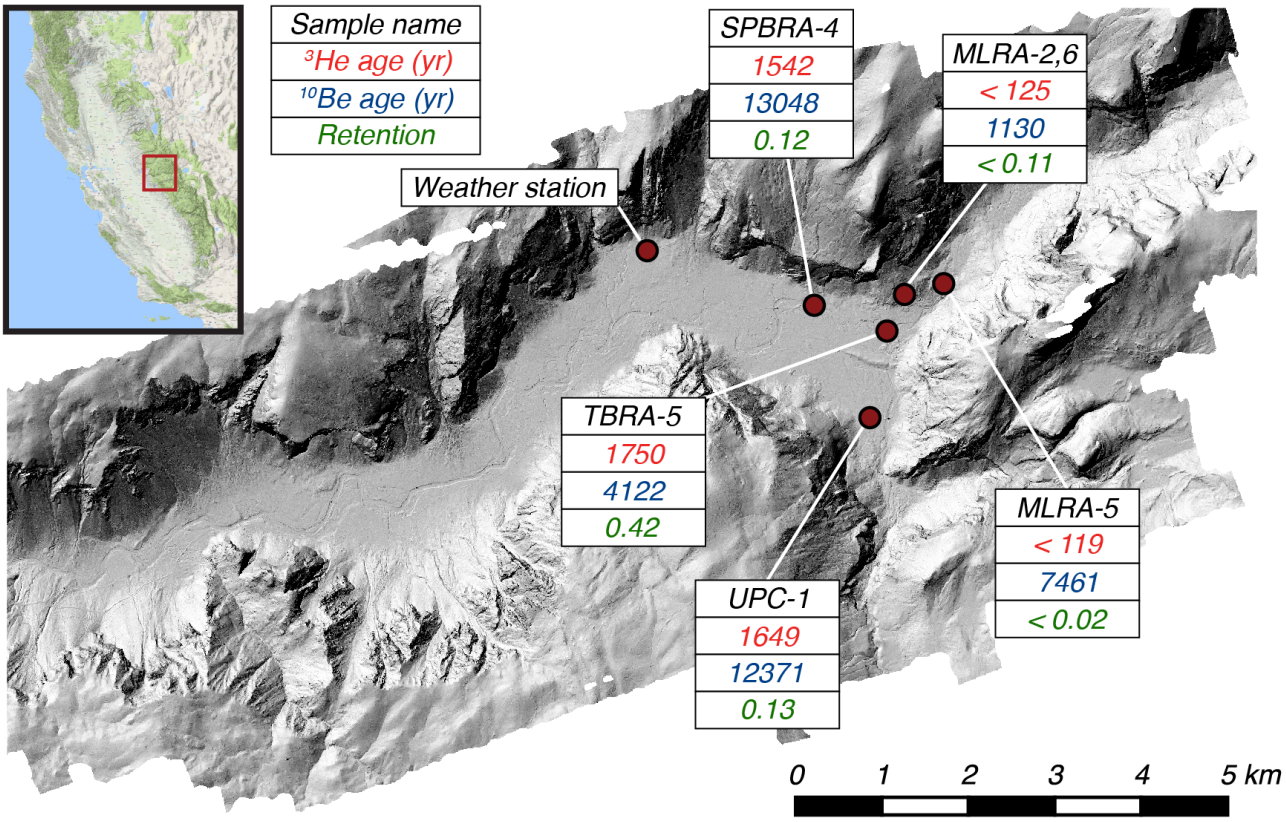

Figures

Figure 1. Light detecting and ranging (LiDAR) map of upper Yosemite Valley showing rock avalanche sample locations and respective ^{3}He and ^{10}Be ages, as well as their observed retention, and the location of the weather station where modern temperature data are collected. Note that MLRA-2,6 and MLRA-5 are near each other, but they are each from a lobe of a separate rockfall event, and have different ^{10}Be exposure ages (Table 2). LiDAR data acquisition and processing for the base map completed by the National Center for Airborne Laser Mapping (NCALM - http://www.ncalm.org). NCALM funding provided by NSF's Division of Earth Sciences, Instrumentation and Facilities Program. EAR-1043051. Topographic map

of California used in location map from Google Maps, 2017.

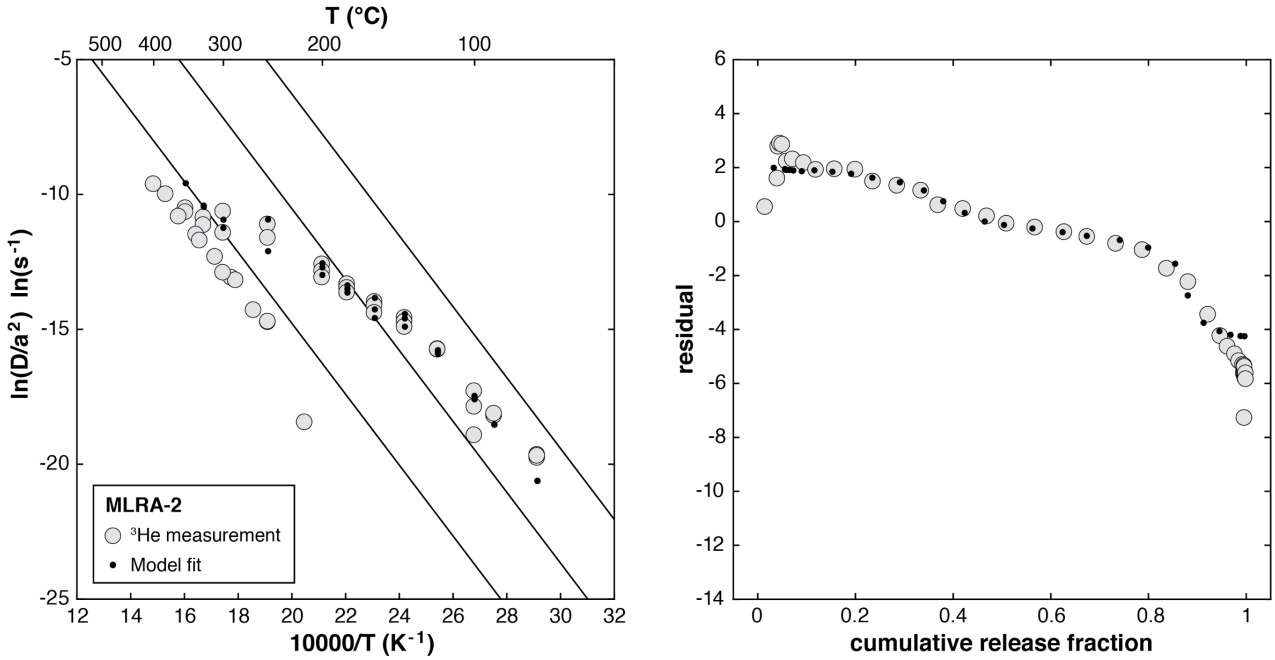

Figure 2. Arrhenius (left) and residual (right) plots for ^{3}He diffusion experiments done on a single fragment of proton-irradiated quartz from sample MLRA-2. The larger grey circles represent data from stepwise degassing experiments, while the smaller black circles represent the predicted diffusivities in a multiple diffusion domain model fit (Table 3). Each line in the Arrhenius plot represents a different diffusion domain for the sample. The slope of each line is proportional to $-E_a$, activation energy, and the y intercept is equal to $ln(D_0/a^2)$, diffusivity at infinite temperature. The residual plotted on the right is a measure of the difference in diffusivities between the diffusion domain that contains the largest fraction of gas, and each measurement and model fit. This residual, on the y axis, is plotted against cumulative fraction of gas released during each heating step, on the x axis.

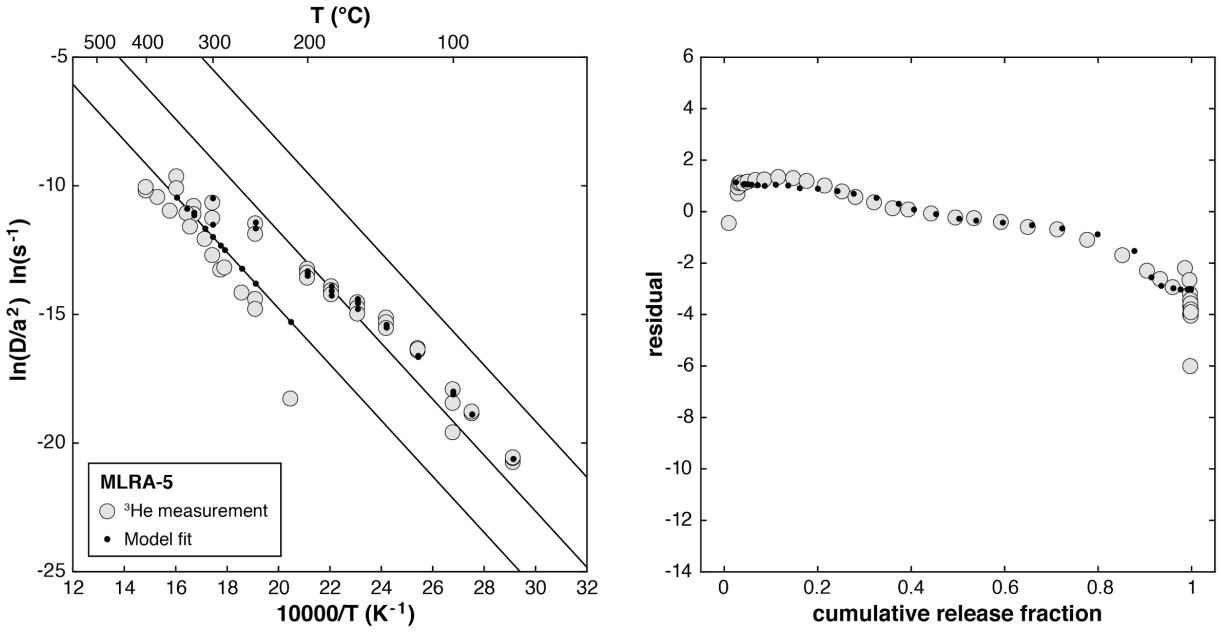

Figure 3. Arrhenius (left) and residual (right) plots for ^{3}He diffusion experiments done on proton-irradiated quartz from sample MLRA-5. All axes, symbols, and lines are same as defined above in Fig. 2., for both plots.

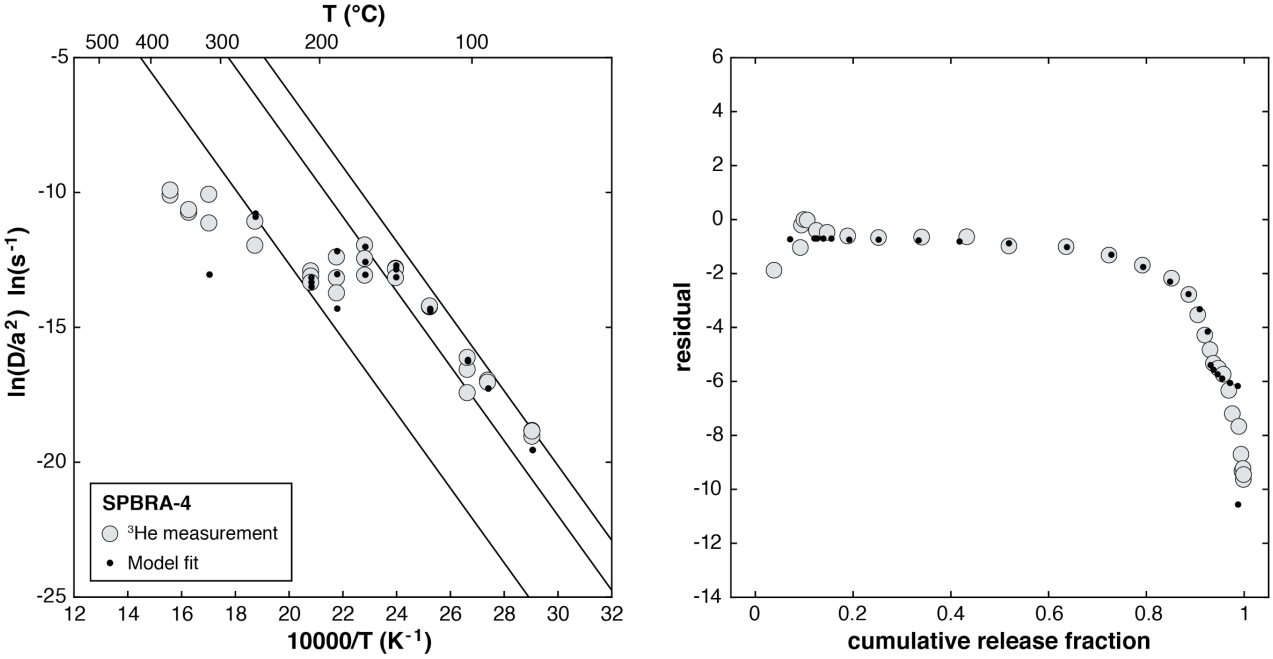

Figure 4. Arrhenius (left) and residual (right) plots for ^{3}He diffusion experiments done on proton-irradiated quartz from sample SPBRA-4. All axes, symbols, and lines

are same as defined above in Fig. 2., for both plots.

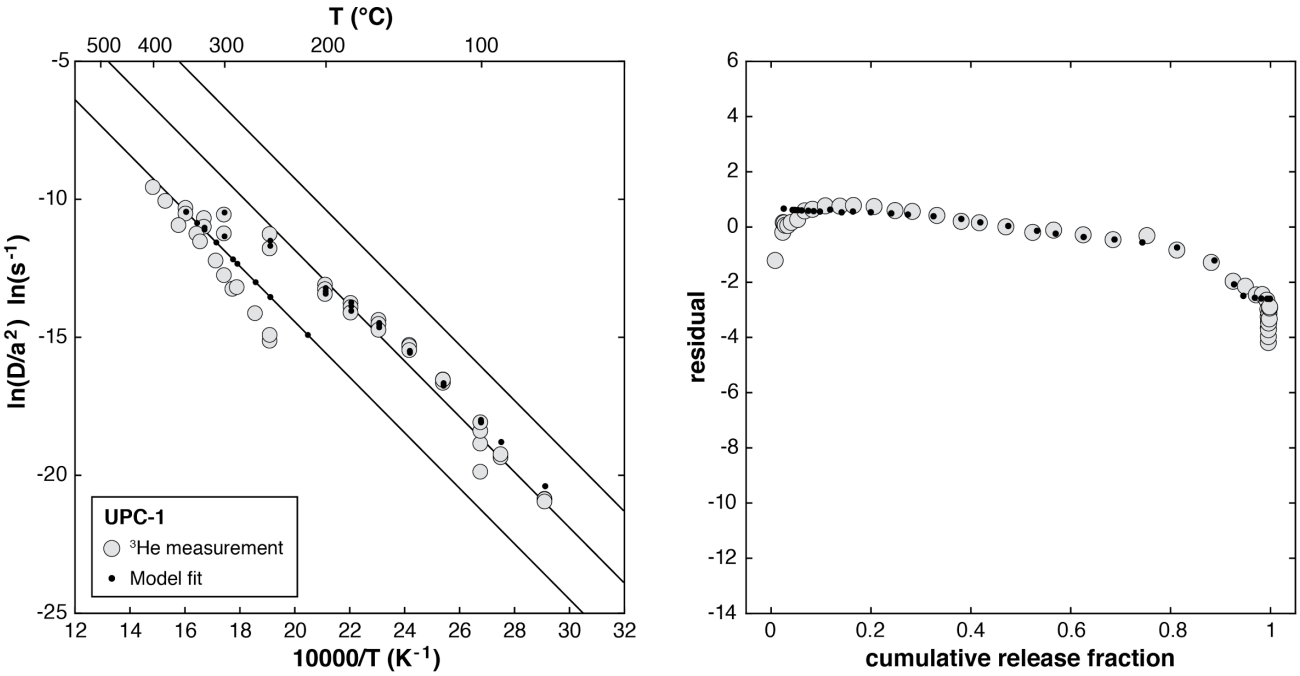

Figure 5. Arrhenius (left) and residual (right) plots for ^{3}He diffusion experiments done on proton-irradiated quartz from sample UPC-1. All axes, symbols, and lines are same as defined above in Fig. 2., for both plots.

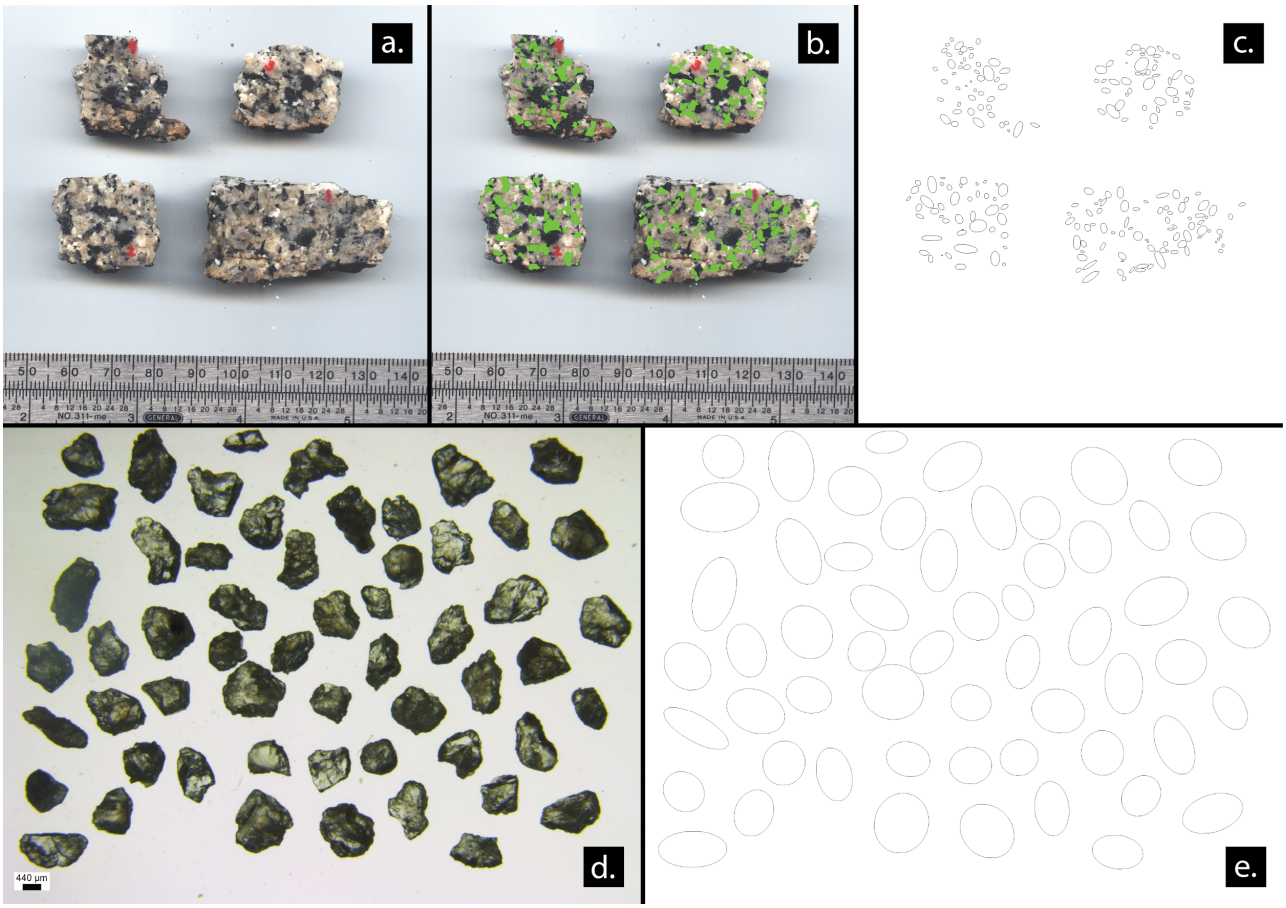

Figure 6. Image processing steps to determine quartz size, shown for sample UPC 1. (a) Raw, scanned "thick-section" image. (b) Grains that can be definitively identified as quartz, traced in green. (c) Equivalent ellipses for thick section drawn by ImageJ during particle analysis. (d) Photomicrograph of crushed quartz separate grains. (e) Equivalent ellipses for photomicrograph drawn by ImageJ during particle analysis.

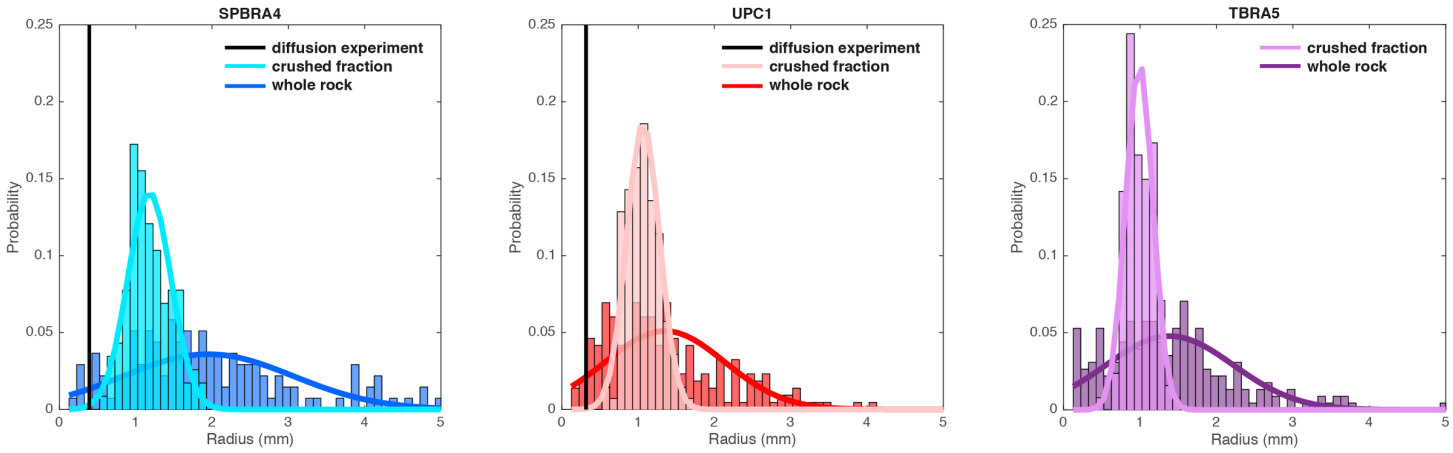

Figure 7. Grain size distribution curves for samples SPBRA-4 (blue), UPC-1 (red), and TBRA-5 (purple). On each plot, a histogram is shown for the spherically equivalent radii of the crushed quartz fraction, and whole-rock grains. Individual columns represent probabilities of finding grains within each size fraction, while the curves overlying each histogram are fit to a normal distribution. The black bars shown for SPBRA-4 and UPC-1 represent the spherically equivalent radius of the single grain used for the diffusion experiment. In each case, the distribution of the crushed fraction grains is narrower than the whole rock grains. This is to be expected, as the crushed fraction is passed through a series of sieves, and the largest single size fraction lacking composite grains is selected for bulk cosmogenic ^{3}He analysis. Figure provided by Marissa Tremblay.

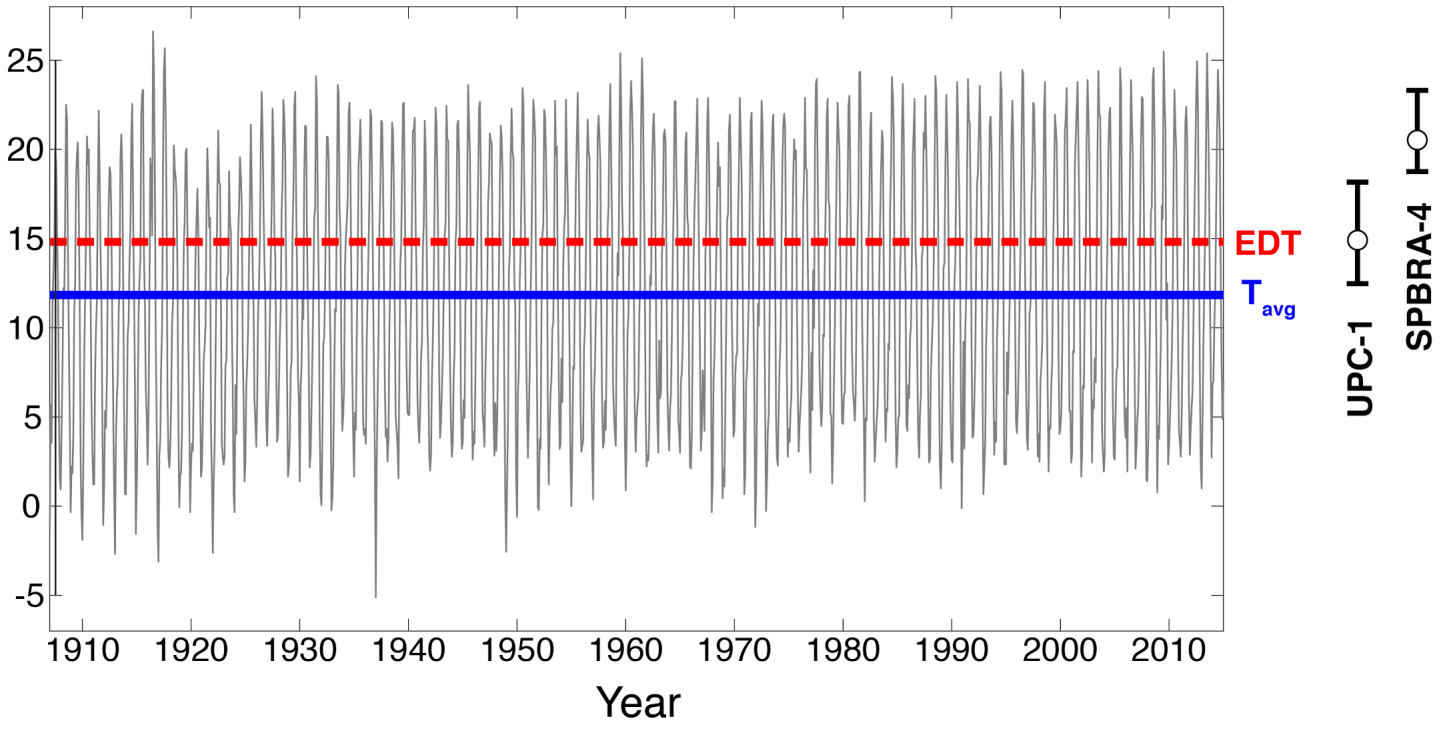

Figure 8. Average monthly temperatures compiled in Yosemite Valley in blue, from 1907 to present. Data are taken from NWS station YPQC1, located at 37.75 N, 119.59 W and shown in Fig. 1. The black solid line represents mean temperature for this time period, while the red dashed line represents the average EDT (see section 1.3). An activation energy of 100 *kj/mol* was used in determining the modern EDT. On the right, mean EDT's for duration of exposure are shown for UPC-1 and SPBRA-4. Uncertainties are shown for each sample, derived from 1-sigma uncertainties in ^{10}Be exposure age and ^{3}He retention. Figure provided by Marissa Tremblay, after own work.

Supplements

Appendix 1. Diffusion experiment data

Appendix 2. Thick section grain size analysis data

Appendix 3. Quartz separate grain size analysis data

Appendix 4. Grain aspect ratio analysis data